Computational Materials Science 96 (2015) 171–177

Contents lists available at ScienceDirect

Computational Materials Science

journal homepage: www.elsevier.com/locate/commatsci

Room temperature multiferroism in $CaTcO_3$ by interface engineering

Hongwei Wang [a,b], Lixin He [a,*], Xifan Wu [b,*]

[a] Key Laboratory of Quantum Information, University of Science and Technology of China, Hefei, Anhui 230026, People's Republic of China
[b] Department of Physics, Temple University, Philadelphia, PA 19122, USA

ARTICLE INFO

Article history:
Received 1 July 2014
Received in revised form 20 August 2014
Accepted 13 September 2014

Keywords:
Multiferroics
Superlattice
Room temperature
Interface engineering

ABSTRACT

We carry out systematic studies of the structural instabilities of the new perovskite family $ATcO_3$ (A = Ca, Sr, Ba) by first-principles calculations. The orthorhombic ground state of $CaTcO_3$ and $SrTcO_3$ are found to be closely related to structural distortions due to the zone boundary phonon instabilities. We also identify a weak ferroelectric instability in $CaTcO_3$, which is however suppressed at the ground state due to the large antiferrodistortive mode. We show that the ferroelectricity in $CaTcO_3$ can be induced in the $CaTcO_3$/$BaTcO_3$ superlattices. Two types of interface mechanisms are involved, one is realized by the mismatch of the antipolar modes between two parent bulk materials and the other is the suppression of antiferrodistortive mode at interface. The Néel temperature of $CaTcO_3$/$BaTcO_3$ superlattices is found to be ~816 K, indicating that $CaTcO_3$ can be engineered into a new room temperature multiferroic material.

1. Introduction

ABO_3 perovskite continues to prove itself to be an important family of multifunctional materials. This is because various instabilities can be simultaneously present within its simple cubic structure at high temperature [1–8]. Many of these instabilities such as magnetic, ferroelectric, antiferrodistortive, and antiferroelectric orderings and their interactions are closely associated with different functionalities that are useful for the device applications [9]. Recently a lot of excitement has been generated, again, in $ATcO_3$ (A = Ca, Sr, Ba) as a new family of perovskite [10–12]. Similar to its isovalent neighbor of Mn ($4s^2 3d^5$), technetium has a $5s^2 4d^5$ electronic configuration with a occupied t_{2g} and empty e_g bands according to the crystal field theory. $ATcO_3$ has the G-type antiferromagnetic (AFM) configuration experimentally [10,12]. Strikingly, $ATcO_3$ is discovered to have an anomalously high magnetic ordering temperature, e.g., the Neél temperature of $CaTcO_3$ is approximately 800 K [10–12], which adopts Pnma space group symmetry all the way below 1273 K [10]. This is in sharp contrast to that of manganese perovskite, in which $CaMnO_3$ only has a Neél temperature of 123 K [13,14].

Progress has already been made in understanding the electronic structures and the magnetic exchange properties in $ATcO_3$ (A = Ca, Sr, Ba) [10–12]. However, the detailed studies of the structural instabilities and their interactions are not yet available in literature. More importantly, keeping this intriguingly high Neél temperature in mind, one might be wondering whether or not more functionalities could be explored in this new family of perovskite.

In this work, we first use the density functional theory (DFT) to perform a systematic investigation of the structural instabilities and distortions in $ATcO_3$ (A = Ca, Sr, Ba). A variety of structural instabilities has been identified. At ground state of $CaTcO_3$ and $SrTcO_3$, the antiferrodistortive (AFD) modes associated with oxygen octahedral rotations are found to originate from the zone boundary phonon instabilities at *M* and *R* points. An antipolar structure is found in $CaTcO_3$ and $SrTcO_3$ originating from the antiferroelectric instability at *X* point and a trilinear coupling with *M* and *R* instabilities that lowers the free energy. An ferroelectric (FE) instability is discovered in only $CaTcO_3$, which is however suppressed by the large AFD mode at the ground state. In the second part, we theoretically investigate the interface induced ferroelectric polarization in $CaTcO_3$/$BaTcO_3$ superlattice. By taking advantage of the intrinsic structural instabilities in $CaTcO_3$, including antipolar and FE ones, we propose that the FE can be induced at the interfaces of the superlattice by two interface engineering approaches. First, the electric polarization can be induced by the mismatch of antipolar structure between $BaTcO_3$ and $CaTcO_3$. Second, the large oxygen octahedral rotation will be suppressed at the interface which can be used to enhance the intrinsic FE mode [15–17]. This picture is confirmed by our DFT calculations and the analysis of $CaTcO_3$/$BaTcO_3$ superlattices. Finally, the Neél temperature of the superlattice is calculated to be ~816 K by a following Monte Carlo simulation. Our theoretical predictions clearly suggest that

* Corresponding authors.
E-mail addresses: helx@ustc.edu.cn (L. He), xifanwu@temple.edu (X. Wu).

http://dx.doi.org/10.1016/j.commatsci.2014.09.011
0927-0256/

the room temperature multiferroism can be achieved in $CaTcO_3$ by interface engineering.

The rest of the paper is organized as follows. Section 2 introduces the technical details of the calculation. Section 3 is devoted into the results and discussions of of in structural instabilities of prototype cubic phase and orthorhombic ground state of bulk $ATcO_3$ (A = Ca, Sr, Ba), followed by describing the induced polarization in $CaTcO_3/BaTcO_3$ superlattices. We summarize in Section 4.

2. Computational methods

Our DFT calculations are done by using the VASP code package [18,19]. In particular, both hybrid functional within the Heyd–Scuseria–Ernzerhof (HSE) scheme [20] and the Perdew–Burke–Ernzerhof functional revised for solids (PBEsol) [21] within the generalized gradient approximation (GGA) are adopted to treat the exchange correlation for electrons. These DFT functionals are known to be very accurate in predicting the volume of solids which is particularly important because the FE instability is sensitive to the cell volume. A 500 eV planewave energy cutoff and $6 \times 6 \times 4$ k mesh points converge very well the results of bulk $ATcO_3$ (A = Ca, Sr, Ba). Ionic coordinates are considered to be fully relaxed until the Hellmann–Feynman force is less then 1 meV/Å. For the superlattices, we use a smaller mesh of $6 \times 6 \times 2$ k points samplings.

In our HSE hybrid functional calculations, a mixing parameter of $a = 0.3$ is adopted. The adoption of mixing parameter in HSE functional is chosen because its closeness in both effective magnetic moment and lattice constant to the experimental values [10,12]. In the calculation based on PBEsol functional, an on-site Coulomb interaction term $U = 3.0$ eV and exchange interaction $J = 1$ eV are used for technetium. Our criterion of choosing the effective on-site Coulomb interaction $U - J$ is based on the matching of results in the lattice constant, band gap, and effective magnetic moment of Tc atoms to those calculated from the accurate HSE hybrid functional.

Our calculations on the cubic $ATcO_3$(A = Ba, Sr, Ca) is based on the $Pm\bar{3}m$ space group symmetry in which the only degree of freedom that allowed to relax is the lattice constant a. In the cubic phase calculations, the main results are based on the GGA + U functional. In calculating the structural ground state of $ATcO_3$(A = Ba, Sr, Ca), both HSE and GGA + U functionals are used, where the symmetry is fixed at the experimentally identified Pnma space group.

In the calculations of $BaTcO_3/CaTcO_3$ superlattices, HSE is only used for the $1BaTcO_3/1CaTcO_3$ short-period superlattice, whereas GGA + U is used in the other longer period superlattices. We carry out DFT calculations for $BaTcO_3/CaTcO_3$ superlattices assuming the coherent growth on the substrate of $GdScO_3$ ($a = 3.97$ Å) [22] and $NdScO_3$ ($a = 4.01$ Å) [23]. The selections of substrates introduce small lattice mismatches by about $\pm 1.26\%$ and $\pm 2.7\%$ in $BaTcO_3$ and $CaTcO_3$ respectively, which are feasible for the experimental growth. The space group symmetry of $BaTcO_3/CaTcO_3$ superlattices is found to be monoclinic (Pc). The ground state structure of superlattice is identified by systematically freezing all the structural instabilities found at cubic phase including octahedral rotations, antipolar, and ferroelectric modes into the supercell with high symmetry, in which a $\sqrt{2}a \times \sqrt{2}a \times c$ is used. Then we perform the structural relaxation including both atomic positions and lattice constant along the superlattice growth direction. Finally, we have also carried out the phonon dispersion computation for the resulting superlattice structures and we found no leftover unstable mode.

To calculate the Neél temperature of the system, we perform Monte Carlo simulations [24] of a Heisenberg model on a $12 \times 12 \times 12$ cubic cell with periodic boundary conditions. Each cubic cell contains four spins. We perform the simulations at temperatures ranging from 300 to 1300 K. At each temperature we carry out an initial 10,000 sweep to prepare the system, sample averages are accumulated over 750,000 sweeps.

3. Results and discussion

3.1. Prototype cubic perovskite structures

In perovskite, the structural instabilities of the prototype cubic phase very often give valuable insights in understanding its low temperature structures and help to analyze its functional properties such as ferroelectricity and multiferroicity [25,26]. To this end, we first relax the structural parameters at cubic phase for $ATcO_3$ (A = Ca, Sr, Ba). In particular, the structural relaxations are performed based on several hypothetical spin configurations, which are G, A, C type antiferromagtic and ferromagnetic spin configurations respectively. The results are presented in Table 1.

It can be seen that for all the $ATcO_3$ under study, the G-type AFM configuration has the lowest total energy. This is also consistent with the G-type AFM magnetic configuration identified experimentally in $CaTcO_3$ and $SrTcO_3$ at room temperature [10,12]. Furthermore, The above results by GGA + U functional are checked by the more accurate HSE hybrid functional. As shown in Table 1, the results obtained from two functionals are quantitatively very close. In particular, both GGA + U and HSE accurately predict the lattice constant of cubic $SrTcO_3$ at 3.967 and 3.948 respectively. In comparison, the experimental value is 3.961 [27].

In Table 2, we present the Born effective charges (Z^*) and the dielectric constant (ϵ_∞) for cubic perovskite $CaTcO_3$, $SrTcO_3$, and $BaTcO_3$. The effective charges on the A site and B site are isotropic; the effective charges of the oxygen atoms can be divided into two independent values, $Z^*_{O\parallel}$ and $Z^*_{O\perp}$, which represent the dynamic charge transfer by perturbing the oxygen atom atom along the O–Tc bond direction and perpendicular to it respectively. Similar to other ABO_3 perovskites, we observe anomalously large $Z^*_{O\parallel}$ resulting from the hybridization between oxygen $2p$ and Tc $4d$ electrons. However, the values are smaller than those in $ATiO_3$ and $AMnO_3$ with $3d$ electrons [28]. This is consistent with the trend

Table 1
Computed cubic $ATcO_3$ (A = Ca, Sr, Ba) structural parameters (Å) and total energy (eV) for different spin configurations with $Pm\bar{3}m$ symmetry. The total energies of G-type AFM structures are chosen to be the references.

		$CaTcO_3$	$SrTcO_3$	$BaTcO_3$
G-AFM	a_0(Å)	3.904	3.967	4.036
	a_0(Å)(HSE)	3.906	3.948	4.022
	Energy (eV)	0.000	0.000	0.000
A-AFM	a_0(Å)	3.913	3.975	4.049
	Energy (eV)	1.065	1.038	0.998
C-AFM	a_0(Å)	3.908	3.970	4.035
	Energy (eV)	0.449	0.448	0.443
FM	a_0(Å)	3.917	3.976	4.048
	Energy (eV)	1.842	1.748	1.637

Table 2
Dielectric constants and Born effective charges (e) of cubic $ATcO_3$ (A = Ca, Sr, Ba) calculated by GGA + U functional. The structures are taken from from results by GGA + U functional in Table 1.

	$CaTcO_3$	$SrTcO_3$	$BaTcO_3$
Z^*_A	2.69	2.66	2.87
Z^*_{Tc}	5.87	5.96	6.19
$Z^*_{O\parallel}$	−5.32	−5.38	−5.61
$Z^*_{O\perp}$	−1.62	−1.62	−1.72
ϵ_∞	8.64	8.60	9.14

of decreasing dynamic charges of B site atoms with 4*d* electrons in perovskite [26].

3.2. Structural instabilities at cubic phase

In Fig. 1, we report the phonon dispersion curves of the cubic $ATcO_3$ (A = Ca, Sr, Ba) along the high symmetry lines of the Brillouin zone. The lowest phonon frequencies at the high symmetry points (Γ, X, M, R) points are also listed in Table 3. In order to check the results by GGA + U, we also report the phonon frequencies by HSE hybrid functional in Table 3. It can be seen that, GGA + U does give qualitatively consistent features compared to those computed from HSE functional [29].

Compared to the structural instabilities in $SrTcO_3$ and $CaTcO_3$, all phonon modes in $BaTcO_3$ are stable. Obviously, in both $SrTcO_3$ and $CaTcO_3$, the largest unstable phonons are M_3^+ and R_5^- modes, which can be identified by the largest imaginary frequencies around 200*i* cm^{-1}. These large *R* and *M* points unstable modes suggest a strong tendency of out-of-phase and in-phase antiferrodistortive (AFD) oxygen octahedral rotation respectively.

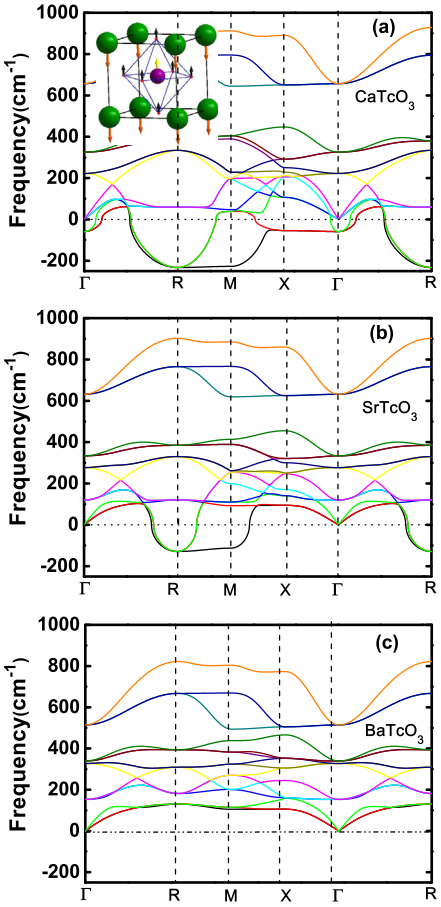

Fig. 1. Phonon dispersions of the cubic $ATcO_3$ (A = Ca, Sr, Ba) along the high-symmetry points, which are computed by GGA + U functional.

Table 3
Computed lowest phonon frequencies (cm^{-1}) of cubic $ATcO_3$ (A = Ca, Sr, Ba) by HSE nybrid functional.

Approach	Material	Γ_4^-	R_5^-	M_3^+	X_5^-
HSE	$CaTcO_3$	58.28*i*	232.39*i*	232.46*i*	53.34*i*
	$SrTcO_3$	118.50	127.81*i*	109.73*i*	94.45
	$BaTcO_3$	151.51	130.44	106.39	103.41
GGA + U	$CaTcO_3$	88.06*i*	221.82*i*	216.48*i*	81.39*i*
	$SrTcO_3$	134.09	152.11*i*	137.43*i*	119.42
	$BaTcO_3$	214.82	141.43	167.12	141.43

The structural distortions due to the M_3^+ and R_5^+ instabilities will be discussed in the next subsection. They give rise to the experimentally identified orthorhombic ground state of Pnma space group symmetry. Besides the AFD instabilities, interestingly, a structural instability X_5^- is also identified at Brillouin zone boundary point (*X*) in $CaTcO_3$. X_5^- mode in $CaTcO_3$ has a smaller imaginary frequency at 53*i* cm^{-1}. The X_5^- mode is an antipolar structural instability and its eigenvector can be described by the Ca and O atoms move in the opposite directions in the CaO layers. The X_5^- structural distortion is also developed at Pnma ground state in $CaTcO_3$ and $SrTcO_3$, which will also be discussed in the next subsection.

However, $CaTcO_3$ exhibits another weak unstable phonon mode Γ_4^- at Brillouin zone center. The Γ_4^- mode is a polar phonon mode, which may generate the electric polarization. The eigenvector of Γ_4^- phonon is depicted in the insert of Fig. 1(a), which can be described by the relative displacement of oxygen octahedral cage and the Ca atom. This particular pattern of ferroelectric phonon instability is refered as the *last* mode in literature [30].

This weak FE instability only exists in $CaTcO_3$ and is absent in either $BaTcO_3$ or $SrTcO_3$. It is well-known that in the conventional perovskite $ATiO_3$ (A = Ba, Sr, Ca), the cubic $BaTiO_3$ has the strongest FE instability and the largest spontaneous polarization at low temperature tetragonal and rhombohedral phases [31]. On the other hand, cubic $CaTiO_3$ has the weakest FE polarization and stays as a paraelectric material at ground state. However, this can be understood by Goldschmidt criterion in terms of the so-called tolerance factor $t = \frac{r_A + r_O}{\sqrt{2}(r_B + r_O)}$ [32]. For comparison, we present the tolerance factor for ABO_3 families with B = Ti, Mn, and Tc respectively in Table 4. According to the Goldsmiths criterion, when $t = 1$, the perovskite prefers the idea cubic structure; when $t > 1$ it prefers the B-site driven ferroelectricity; when $t < 1$ the perovskite prefers both the A-site driven ferroeletricity and oxygen octahedral rotation at the same time. Because the radius of Tc is larger than that of Ti, the tolerance factor in $BaTcO_3$ is very close to 1 favoring the idea cubic structure; on the other hand, the tolerance factor of $BaTiO_3$ is larger than 1 favoring the B-site driven ferroelectricity. This is consistent with the absence of any structural instability in $BaTcO_3$.

Similar weak FE instabilities are also found in other perovskite materials, such as $CaMnO_3$ [33] and $CaTiO_3$ [34]. However, the electric polarization is not able to develop in these materials because they are suppressed by the large oxygen octahedral rotation AFD modes, which is in strong competition with FE modes. In Section 3.4, we will discuss how to induce the FE by interface engineering method in superlattices.

3.3. Pnma ground state

In experiments, the only available low symmetry structures found in $CaTcO_3$ and $SrTcO_3$ are the orthorhombic structures with Pnma space group symmetry [10,12]. The structural distortions from cubic to orthorhombic phase can be viewed as the combined condensations of the R_5^- and M_3^+ zone boundary unstable phonon modes. As a result, in the Pnma structure, the oxygen octahedral exhibits out-of-phase rotation around [110] axis and in-phase oxygen rotation around [001] axis. In Glazer notation [35], they are referred to as $a^-a^-c^0$ and $a^0a^0c^+$ type oxygen rotations respectively. Following the convention in literature [36], we refer the oxygen octahedral rotation around [001] as *rotation* and refer oxygen octahedral rotation around [001] axis as *tilting* in the following paragraphs.

Table 4
Computed tolerance factors (t) of typical perovskite-type oxides ABO_3 (with A = Ba, Sr, Ca and B = Ti, Mn, Tc).

	$CaTcO_3$	$SrTcO_3$	$BaTcO_3$
t	0.914	0.947	1.004
	$CaTiO_3$	$SrTiO_3$	$BaTiO_3$
t	0.966	1.002	1.062
	$CaMnO_3$	$SrMnO_3$	$BaMnO_3$
t	0.959	0.994	1.054

In Table 5, we present the relaxed orthorhombic structure of $ATcO_3$ (A = Ba, Sr, Ca) with Pnma space group symmetry, in which the available experimental structures are also presented for comparison. It can be seen that the HSE hybrid functional accurately reproduces the experimental structures. On the other hand, the PBEsol functional slightly overestimates the lattice constants and volumes, which are typical for the GGA approximation of exchange correlation functionals.

It is worth to note that with the increasing radius of *A* site atoms, the rotational and tilting angles are decreasing from very large angle in $CaTcO_3$ to almost zero in $BaTcO_3$ as shown in Table 5. At the same time, the crystal structures also change from being strongly orthorhombic in $CaTcO_3$ to being cubic symmetry in $BaTcO_3$. Indeed, the above trend is consistent with the Goldschmidt criterion in terms of the increasing structural factors as we have discussed in the previous subsection.

Except for the zone boundary R_5^- and M_3^+ structural modes that generate the Pnma ground state structure, it is also interesting to note that the other less unstable structural instability, X_5^-, is also condensed in orthorhombic $CaTcO_3$ and $SrTcO_3$ generating the antipolar structure. This induced antipolar structure can be understood by the trilinear coupling term $\sim \lambda Q_{R_5^-} Q_{M_3^+} Q_{X_5^-}$ in the free energy phenomenologically [37,38]. As shown in Fig. 2(a), when only X_5^- structural distortion is frozen into the $CaTcO_3$, the total energy starts with a shallow double-well potential. This is consistent with the weak X_5^- phonon instability as discussed in previous subsection. However, when both R_5^- and M_3^+ structural distortions are present, the resulting energy is much lower. The resulting single-well potential profile indicates that the antipolar structure is induced improperly by the trilinear coupling in the free energy term, as shown in Fig. 2(d).

Unfortunately, the FE structural instability at cubic phase although has similar imaginary frequency to X_5^-, is not condensed at Pnma ground state. This is due to the strong competition between FE and oxygen octahedral rotation [15,39]. In the end, we have recalculated the phonon dispersion for all the $ATcO_3$ materials in the orthorhombic phase and no unstable mode is found any more indicating that the we have found the ground state structures theoretically.

3.4. Induced ferroelectricity by interface design in proposed $BaTcO_3$/$CaTcO_3$ superlattice

In this subsection, we focus on the discussion of the induced FE in $CaTcO_3$ by possible material engineering methods. In particular, we are going to take advantage of two intrinsic structural instabilities in cubic $CaTcO_3$, i.e. X_5^- and Γ_4^-, which are antipolar and polar modes respectively. The antipolar structural distortion is present at the orthorhombic ground state, while the polar one is not due to the large AFD octahedral rotations. With the intriguingly high Neél temperature found in $CaTcO_3$, it is particularly desirable that the FE polarization could be recovered and turned into a new room temperature multiferroic material.

The above can be achieved in the artificial materials based on modern thin-film technology. In general, there are two approaches, which are the *epitaxial strain* and *interface engineering* methods respectively. We first try the epitaxial strain method. By using the coupling between polar instability and epitaxial strain applied by the substrate, the epitaxial strain has been very often used to induce the FE in other perovskite materials [40]. To do so, we apply both tensile and compressive strain on the cubic $CaTcO_3$ systematically in the range of $\pm \sim 5\%$. At the same time, we lower the space group symmetry in the calculations to allow the development of polarization along both *c* axis and in the *ab* plane. Unfortunately, our calculations show that $CaTcO_3$ persists to be paraelectric even as much as $\pm 5\%$ has been applied.

We then focus on the possibility of interface engineering. Compared with epitaxial strain, more dramatic changes in the strengths of instabilities can be achieved at the interfaces resulting in an overall change of functionalities [15–17,41]. We propose that the FE can be induced by the interfaces of the $CaTcO_3/BaTcO_3$ superlattices. In particular, two types of interface engineering mechanisms are expected to take place that have been demonstrated recently in the literature [15,42]. First, FE can be induced by the mismatch of antipolar instabilities of two parent Pnma perovskites. This mismatch brings out a finite polarization at the interface due to the non-varnishing cancellation of antipolar moment. In literature, this is the so-called *improper* induced FE, because the antipolar in bulk is induced by the other two structural distortions R_5^- and M_3^+ according to the trilinear coupling term $\sim \lambda Q_{R_5^-} Q_{M_3^+} Q_{X_5^-}$ in free energy as discussed in the previous subsection [37,38]. With a large antipolar structural distortion in $CaTcO_3$ and an almost cubic $BaTcO_3$, it can be expected that the electric dipole moment can be maximized at the interface of $CaTcO_3/BaTcO_3$ superlattices. Secondly, it has been recently shown that a substantial reduction of AFD associated with octahedral rotations at the interface layer of $CaTiO_3/BaTiO_3$ can be used to enhance the FE [15]. This is the so-called induced *proper* FE since it originates from the softening of intrinsic polar instability, e.g. Γ_4^- in cubic perovskite. Based on the same reasoning, we expect that the similar reduction of AFD mode will occur at the interface of $CaTcO_3/BaTcO_3$, which will further enhance the polarization. As a result, it will be very interesting to check if FE can be induced in the $CaTcO_3/BaTcO_3$ short-period superlattices by the above comprehensive interface engineering mechanisms.

We assume the coherent growth of $BaTcO_3/CaTcO_3$ superlattices on the substrate of $GdScO_3$ as schematically shown in Fig. 3. The first principles' results are summarized in Table 6. As one of the key results, the $1BaTcO_3/1CaTcO_3$ superlattice does exhibit a FE ordering with a spontaneous polarization $P_s = 5.92\ \mu c/cm^2$ by HSE func-

Table 5
Theoretically computed structural parameters, magnetic exchange angles (°) [11], oxygen octahedral rotation angles ϕ_r(°), and tilting angles ϕ_t(°) of ground state $ATcO_3$ (A = Ca, Sr, Ba) with Pnma symmetry. The available experimental values [11] are also shown in parenthesis.

		a(Å)	b(Å)	c(Å)	V(Å^3)	Tc − $\widehat{O_1}$ − Tc	Tc − $\widehat{O_2}$ − Tc	ϕ_r	ϕ_t
Pnma (HSE)	$CaTcO_3$	5.53 (5.53)	7.71 (7.70)	5.39 (5.39)	230.05 (229.15)	150.90 (150.43)	150.91 (151.53)	10.04	14.55
	$SrTcO_3$	5.56 (5.54)	7.86 (7.85)	5.61 (5.58)	244.92 (242.74)	163.39 (161.57)	167.76 (166.96)	0.60	8.32
	$BaTcO_3$	5.69	8.05	5.67	260.20	179.96	179.90	0.049	0.019
Pnma (GGA + U)	$CaTcO_3$	5.57 (5.53)	7.73 (7.70)	5.41 (5.39)	232.08 (229.15)	148.41 (150.43)	148.91 (151.53)	10.63	15.80
	$SrTcO_3$	5.59 (5.54)	7.90 (7.85)	5.60 (5.58)	247.51 (242.74)	161.13 (161.57)	161.24 (166.96)	6.18	9.13
	$BaTcO_3$	5.71	8.08	5.71	262.87	179.94	179.88	0.058	0.032

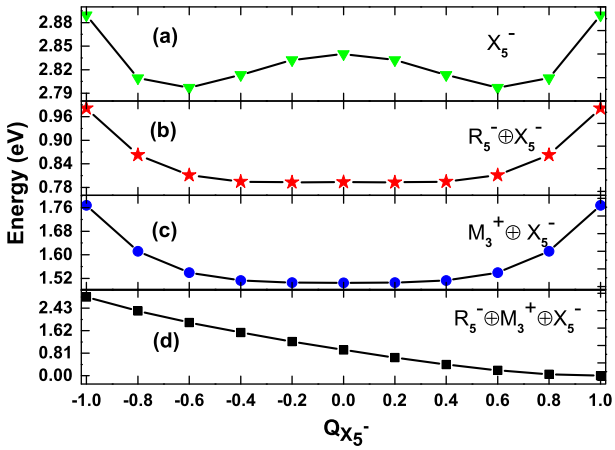

Fig. 2. Energies profiles in $CaTcO_3$ as functions of mode amplitudes with frozen (a) $Q_{X_5^-}$ only, (b) both $Q_{R_5^-}$ and ground state mode amplitude of $Q_{X_5^-}$, (c) both $Q_{X_5^-}$ and ground state mode amplitude of $Q_{M_3^+}$, (d) $Q_{X_5^-}$, and ground state mode amplitudes of $Q_{R_5^-}$, $Q_{M_3^+}$. The normalization factor 1 is chosen by the mode amplitude (Q) at relaxed Pnma ground state in Table 5.

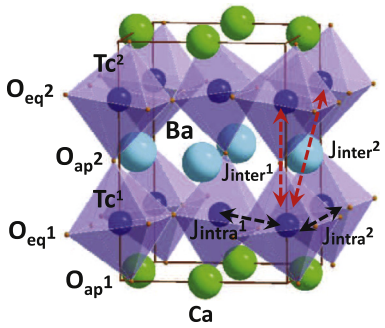

Fig. 3. Schematic atomic structure of relaxed $1CaTcO_3/1BaTcO_3$ superlattice at theoretical DFT ground state with monoclinic space group symmetry Pc.

tional (or similarly 6.34 μc/cm² by PBEsol functional) along the [1 1 0] in-plane axis. On the other hand, the pure $CaTcO_3$ grown on the same substrate does not exhibit any FE structural instability.

The emergence of FE ordering only in superlattice suggests that it is an interface effect. In order to further elucidate its interfacial origin, we employ the layer polarization decomposition to analyze the local polarization profile based on linear approximation [28] as shown in Table 6. In strained bulk $CaTcO_3$, the local polarization profile is dominated by the clear antipolar ordering [42]. The relative displacement of Ca and O atom in the same plane generates a large dipole along [1 1 0] and [$\bar{1}\,\bar{1}$ 0] directions in alternate layers resulting a zero total polarization [42]. In superlattices, this large antipolar type local polarization $\sim 27.6\ \mu c/cm^2$ is preserved in the chemical environment, in which CaO is sandwiched by two TcO_6 octahedra. However, its magnitude is also perturbed at the interfaces as shown in Table 6. The local polarizations of CaO layer in 3:3 superlattice can be divided into two categories, bulk p_{CTO} and interfaces of type I (p_{in}^{I}), which is defined by the local polarization of a CaO layer with one BaO layer as neighbor. One can see that the p_{CTO} in 3:3 superlattice is almost the same value as that in strained bulk $CaTcO_3$. The p_{in}^{I} is smaller than p_b, which is due to the suppressed oxygen rotations and tilting at the interface. In 2:2 superlattice, there is only one type of local polarization profile of CaO layer which belongs to interface type-I and p_{in}^{I} has a similar magnitude as that of 3:3 superlattice indicating the same chemical environment. However, in 1:1 superlattice, CaO layer is dominated by the type-II interfaces, in which the CaO layer is sandwiched by two BaO layers. This is in qualitatively difference with interface of longer period superlattices resulting in that $p_{in}^{II} < p_{in}^{I}$. A question arises: how we could understand the two different local polarization of interfacial CaO layers in one unified picture? We describe the interface effect on the local polarization by perturbation theory. It can be further assumed that the magnitude of perturbation is within the linear regime, in which p_{in}^{I} (p_{in}^{II}) are only different from the bulk value by the perturbations introduced by the suppressed AFE ordering from one (two) neighboring BaO layers. Thus, one can arrive at $p_{in}^{II} = p_{CTO} - 2 \times (p_{CTO} - p_{in}^{I}) \sim 19\ \mu c/cm^2$. This is very close 19.38 μc/cm² obtained from the actual DFT calculation.

The above local profile analysis clearly indicates that a large part of the interface induced FE is from the mismatch of antipolar distortion (X_5^- mode). The X_5^- phonon mode can be described as the atomic displacements along [1 1 0] direction including only the A site atoms and the apical oxygen atoms O_{ap} in the same layer. However, the local analysis also shows that the AFD is largely suppressed at the interfaces. Therefore, a proper FE contribution can be also expected from the induced polarization. The proper FE originates from the zone center Γ_4^- in cubic perovskite and transforms into Γ_5^- with lower space group symmetry Pc in the supperlattices. The displacement of proper FE can be computed by the first-principles calculations in 1:1 superlattice with space group symmetry P4mm, in which the octahedral rotation and tilting are completely eliminated. As shown in Table 7, the proper FE mode displacement includes all the O_{ap}, equatorial oxygen O_{eq}, and A site atoms moving along [1 1 0] directions. Based on the modes's difference between improper and proper, we then performed the polarization mode decompositions into proper and improper contributions as shown in Table 7. Indeed, it can be seen that the improper polarization comprises the major part (78%) of the induced polarization, while the proper one contributes to the 22% rest of induced polarization. It can also be seen that the M_5^- and the M_3^+ representing the $a^0a^0c^-$ and $a^-a^-c^0$ type oxygen octahedral rotations do not have any contribution to induced polarization. This is consistent with the AFD nature of these oxygen rotations. The induced proper ferroelectricity is of particular interest. This is because it is associated with Tc ions, which are also responsible for the magnetism in these materials. Therefore, it is possible to achieve strong magnetoelectric coupling in the $CaTcO_3/BaTcO_3$ short-period superlattices [16,17].

Interestingly, with both the proper and improper polarization at the interface, it is possible that the proper polarization can be further engineered by the epitaxial strain. In perovskite materials, such as $SrTiO_3$ and $CaTiO_3$, the [1 1 0] in-plane polarization can be increased by applying tensile epitaxial strains. As shown in Table 7, we report the same mode decomposition of induced polarization for a larger tensile strain on $NdScO_3$ substrate. It can be seen that under this additional tensile strain, the displacement of equatorial oxygen O_{eq} is greatly increased. As a result, the induced proper polarization is also magnified by a factor of two. At the same time, we see a reduction of the improper contribution to the induced polarization. This is due to the smaller in oxygen octahedral rotation and tilting angles. It should be reminded that the effect of strain engineering is absent in bulk $CaTcO_3$. This additional strain tunability of polarization further confirm that the interface induced polarization is of both proper and improper properties. Since the polarization of $nBaTcO_3/nCaTcO_3$ is induced by interface, the maxium polarization is achieved in the shortest period superlattice, i.e. $1BaTcO_3/1CaTcO_3$, in which the interfaces are the densest.

Both $BaTcO_3$ and $CaTcO_3$ have been found to have high Neél temperature well above room temperature. It has been argued that the more delocalized 4*d* orbital enhance the covalent hybridization with neighboring oxygen atoms, which in turn increase the hopping matrix according to the Anderson–Goodenough–Kanamori rules [10,44]. Therefore, it can be expected that the large magnetic

Table 6
Layer-by-layer decompositions of polarization p(μc/cm^2), oxygen octahedral rotation angles ϕ_r(°), and tilting angles ϕ_t(°) in the superlattices of 1$BaTcO_3$/1$CaTcO_3$(1:1), 2$BaTcO_3$/2$CaTcO_3$(2:2), 3$BaTcO_3$/3$CaTcO_3$(3:3), and strained bulk $CaTcO_3$ (CT^s) and $BaTcO_3$(BT^s). The calculations are based on by GGA + U functional. The layer polarization is based on the definition centered on AO plane [43].

		CaO_i^I	TiO_2	CaO_b	TiO_2	CaO_i^I	TiO_2	BaO_i^I	TiO_2	BaO_b	TiO_2	BaO_i^I	TiO_2
3:3													
	p_{110}	−23.11	–	27.58	–	−23.27	–	2.61	–	−0.33	–	2.72	–
	p_{001}	−5.85	–	−0.02	–	5.82	–	2.53	–	0.034	–	−2.48	–
	ϕ_r	–	9.34	–	9.20	–	6.38	–	−0.24	–	−0.33	–	6.14
	ϕ_t	–	15.83	–	15.82	–	9.30	–	2.78	–	2.77	–	9.30
	P_{110}^{total} = 2.28					P_{001}^{total} = 0.00							
2:2													
	p_{110}	−22.10	–	–	–	23.39	–	−2.85	–	–	–	2.91	
	p_{001}	−5.55	–	–	–	5.57	–	2.73	–	–	–	−2.65	
	ϕ_r	–	9.76	–	–	–	5.79	–	–	–	0.46	–	5.77
	ϕ_t	–	14.62	–	–	–	9.51	–	–	–	4.38	–	9.50
	P_{110}^{total} = 0.068					P_{001}^{total} = 0.00							
		CaO_i^{II}	TiO_2	BaO_i^{II}	TiO_2								
1:1													
	p_{110}	19.38	–	−6.12	–								
	p_{001}	0.02	–	0.04	–								
	ϕ_r	–	5.82	–	5.94								
	ϕ_t	–	9.41	–	9.41								
	P_{110}^{total} = 6.34					P_{001}^{total} = 0.03							
		CaO_i^{II}	–	–	BaO_i^{II}	–	–						
1:1 HSE													
	p_{110}	15.60	–	–	−4.39	–	–						
	p_{001}	0.04	–	–	0.08	–	–						
	P_{110}^{total} = 5.92					P_{001}^{total} = 0.06							
		–	CaO_b	–	CaO_b	–	–						
CT^S													
	p_{110}	–	27.57	–	−27.58	–	–						
	p_{001}	–	0	–	0	–	–						
		–	BaO_b	–	BaO_b	–	–						
BT^S													
	p_{110}	–	0	–	0	–	–						
	p_{001}	–	0	–	0	–	–						

Table 7
The mode decomposition of the $(CaTcO_3)_1/(BaTcO_3)_1$ superlattices of relaxed theoretical ground state with space group Pc grown on $GdScO_3$ and $NdScO_3$ substrates. The first-principles results are based on HSE hybrid functional.

	$GdScO_3$ substrate (3.97 Å)					$NdScO_3$ substrate (4.01 Å)				
	Γ_5^- (total)	Γ_5^- (proper)	Γ_5^- (improper)	M_5^-	M_3^+	Γ_5^- (total)	Γ_5^- (proper)	Γ_5^- (improper)	M_5^-	M_3^+
Ca	0.2466	0.0393	0.2073	-	-	0.2520	0.0725	0.1795	-	-
Ba	−0.0841	−0.0019	−0.0822	-	-	−0.0757	−0.0037	−0.0720	-	-
Tc^1	−0.0034	−0.0034	-	-	-	−0.0035	−0.0035	-	-	-
Tc^2	−0.0041	−0.0041	-	-	-	−0.0035	−0.0035	-	-	-
O_{ap}^1	−0.1367	−0.0177	−0.1190	-	0.5487	−0.1380	−0.0301	−0.1079	-	0.5635
O_{ap}^2	0.0018	0.0006	0.0012	-	0.2677	0.0042	0.0009	0.0033	-	0.2823
O_{eq}^1	−0.0057	−0.0057	-	0.3486	0.4260	−0.0130	−0.0130	-	0.2772	0.4352
O_{eq}^2	−0.0072	−0.0072	-	0.3361	0.4270	−0.0123	−0.0123	-	0.2769	0.4357
Q_{total} (Å)	0.2944	0.0444	0.2527	0.4842	0.8582	0.2977	0.0807	0.2214	0.3918	0.8811
P (μC/cm^2)	5.92	1.31	4.61	-	-	6.70	2.79	3.91	-	-

antiferromagnetic coupling will be kept in the $BaTcO_3/CaTcO_3$ superlattices. To further confirm this, we map the total energies in different magnetic configurations onto the Heisenberg Hamiltonian [4]

$$H = -\sum_{ij} J_{ij} S_i \cdot S_j. \quad (1)$$

The exchange coupling constants include the nearest-neighbor (J^1) and next -nearest-neighbor (J^2), beyond which the coupling constant is found to be very small and could be neglected. This coupling constants are further decomposed into the contributions from intralayer (J_{intra}) and interlayers (J_{inter}). The results are listed in Table 8. One can see that the exchange coupling constants are approximately the averages of those of the bulk $BaTcO_3$ and bulk $CaTcO_3$ in both intra- and inter- layer contributions. We obtain the AFM phase transition at 816 K from the Monte Carlo simulation. Furthermore, as explained in previous paragraphs, the mechanism of induced ferroelectric dipole moment is due to the non-cancellation of anti-polar moments from $CaTcO_3$ and $BaTcO_3$ at the interface layer in the superlattices. The Pnma structural phase transition temperature in $CaTcO_3$ has been experimentally determined to be at 1273 K [10]. The structural phase transition in BaT-

Table 8
Effective magnetic moments $m(\mu_B)$, exchange coupling constants J(meV), and Neél temperature T_N(K) of bulk $CaTcO_3$, bulk $BaTcO_3$, and $1CaTcO_3/1BaTcO_3$ superlattice. GGA + U functional is used in the DFT calculations.

	$CaTcO_3$	$BaTcO_3$	$1CaTcO_3/1BaTcO_3$
m	2.14	2.09	2.05
J^1_{inter}	−38.10	−69.02	−52.60
J^1_{intra}	−38.10	−69.02	−60.29
J^2_{inter}	−0.78	−1.09	−2.89
J^2_{intra}	−0.78	−1.09	−3.17
T_N	602	1089	816

cO_3 has not been reported yet. This is consistent with our DFT results which show no unstable phonon mode, indicating $BaTcO_3$ stays cubic structure at room temperature. Therefore, the above experimental and theoretical facts suggest that $CaTcO_3/BaTcO_3$ should be multiferroic at room temperature.

4. Conclusion

Based on accurate first-principles calculations, we have performed careful studies of structural instabilities for the recently discovered perovskite $ATcO_3$ (A = Ba, Sr, Ca). The experimental structures in $CaTcO_3$ and $SrTc_3$ are elucidated by the distortions originating from the structural instabilities and their couplings at prototype cubic phases. Based on the distinct structural instabilities in $CaTcO_3$ and $BaTcO_3$, we propose and show that the electric polarization can be induced by the interfaces in $BaTcO_3/CaTcO_3$ superlattices, in which comprehensive interface engineering mechanisms are taken into account. The theoretically proposed superlattice is found to be a new room-temperature multiferroic and await for future experimental confirmation.

Acknowledgments

This work is supported in part by Air Force Office of Scientific Research under award numbers FA9550–13-1–0124 (X. Wu). L. He acknowledge the support from the Chinese National Fundamental Research Program 2011CB921200, National Natural Science Funds for Distinguished Young Scholars and CNSF Grant No. 11374275. X. Wu acknowledges the computational support by the National Science Foundation through TeraGrid resources provided by NICS under Grant No. [TG-DMR120045] and the National Energy Research Scientific Computing Center (NERSC).

References

[1] H.Y. Hwang, Y. Iwasa, M. Kawasaki, B. Keimer, N. Nagaosa, Y. Tokura, Nat. Mater. 11 (2012) 103.
[2] J. Hong, D. Vanderbilt, Phys. Rev. B 87 (2013) 064104.
[3] J.W. Bennett, K.F. Garrity, K.M. Rabe, D. Vanderbilt, Phys. Rev. Lett. 110 (2013) 017603.
[4] J.H. Lee, K.M. Rabe, Phys. Rev. B 84 (2011) 104440.
[5] J.H. Lee, K.M. Rabe, Phys. Rev. Lett. 107 (2011) 067601.
[6] A. Malashevich, D. Vanderbilt, Phys. Rev. Lett. 101 (2008) 037210.
[7] A. Roy, M. Stengel, D. Vanderbilt, Phys. Rev. B 81 (2010) 014102.
[8] J.Y. Jo, R.J. Sichel, H.N. Lee, S.M. Nakhmanson, E.M. Dufresne, P.G. Evans, Phys. Rev. Lett. 104 (2010) 207601.
[9] C.H. Ahn, K.M. Rabe, J.M. Triscone, Science 303 (2004) 5657.
[10] M. Avdeev, G.J. Thorogood, M.L. Carter, B.J. Kennedy, J. Ting, D.J. Singh, K.S. Wallwork, J. Am. Chem. Soc. 133 (2011) 1654.
[11] C. Franchini, T. Archer, J. He, X. Chen, A. Filippetti, S. Sanvito, Phys. Rev. B 83 (2011) 220402.
[12] E.E. Rodriguez, F. Poineau, A. Llobet, B.J. Kennedy, M. Avdeev, G.J. Thorogood, M.L. Carter, R. Seshadri, D.J. Singh, Anthony K. Cheetham, Phys. Rev. Lett. 106 (2011) 067201.
[13] H. Taguchi, Phys. Stat. Sol. 88 (1985) K79.
[14] T. Günter, E. Bousquet, A. David, Ph. Boullay, Ph. Ghosez, W. Prellier, M. Fiebig, Phys. Rev. B 85 (2012) 214120.
[15] X. Wu, K.M. Rabe, D. Vanderbilt, Phys. Rev. B 83 (2011) 020104.
[16] H. Wang, L. He, X. Wu, Europhys. Lett. 100 (2012) 17005.
[17] C. Swartz, X. Wu, Phys. Rev. B 85 (2012) 054102.
[18] G. Kresse, J. Hafner, Phys. Rev. B 47 (1993) R558.
[19] G. Kresse, J. Furthmuller, Phys. Rev. B 54 (1996) 11169.
[20] J. Heyd, G.E. Scuseria, M. Ernzerhof, J. Chem. Phys. 118 (2003) 8207.
[21] J.P. Perdew, A. Ruzsinszky, G.I. Csonka, O.A. Vydrov, G.E. Scuseria, L.A. Constantin, X.L. Zhou, K. Burke, Phys. Rev. Lett. 100 (2008) 136406.
[22] K.M. Rabe, C.H. Ahn, J.-M. Triscone (Eds.), Physics of Ferroelectrics: A Modern Perspective, Springer, Berlin, 2007.
[23] R. Uecker, B. Velickov, D. Klimm, R. Bertram, M. Bernhagen, M. Rabe, M. Albrecht, R. Fornari, D.G. Schlom, J. Crystal Growth 310 (2008) 2649–2658.
[24] Kun Cao, Guang-Can Guo, David Vanderbilt, Lixin He, Phys. Rev. Lett. 103 (2009) 257201.
[25] J.B. Neaton, C. Ederer, U.V. Waghmare, N.A. Spaldin, K.M. Rabe, Phys. Rev. B 71 (2005) 014113.
[26] S. Amisi, E. Bousquet, K. Katcho, P. Ghosez, Phys. Rev. B 85 (2012) 064112.
[27] G.J. Thorogood, M. Avdeev, M.L. Carter, B.J. Kennedy, J. Ting, K.S. Wallwork, Dalton Trans. 40 (2011) 7228–7233.
[28] X. Wu, O. Diéguez, K.M. Rabe, D. Vanderbilt, Phys. Rev. Lett. 97 (2006) 107602.
[29] J. Hong, A. Stroppa, J. Íniguez, S. Picozzi, D. Vanderbilt, Phys. Rev. B 85 (2012) 054417.
[30] J.T. LAST, Phys. Rev. 105 (1957) 6.
[31] X. Wu, D. Vanderbilt, D.R. Hamann, Phys. Rev. B 72 (2005) 035105.
[32] V.M. Goldschmidt, Die Gesetze der Krystallochemie, Die Naturwissenschaften, 21 (1926) 477.
[33] S. Bhattacharjee, E. Bousquet, P. Ghosez, Phys. Rev. Lett. 102 (2009) 117602.
[34] C.J. Eklund, C.J. Fennie, K.M. Rabe, Phys. Rev. B 79 (2009) 220101. R.
[35] A.M. Glazer, Acta Cryst. B28 (1972) 3384.
[36] A.M. Glazer, Acta Cryst. A31 (1975) 756.
[37] J.M. Rondinelli, C.J. Fennie, Adv. Mater. 24 (2012) 1961–1968.
[38] N.A. Benedek, A.T. Mulder, C.J. Fennie, J. Solid State Chem. 195 (2012) 11–20.
[39] W. Zhong, D. Vanderbilt, Phys. Rev. Lett. 74 (1995) 2587.
[40] O. Diéguez, K.M. Rabe, D. Vanderbilt, Phys. Rev. B 72 (2005) 144101.
[41] E. Bousquet et al., Nature(London) 452 (2008) 732.
[42] A.T. Mulder, N.A. Benedek, J.M. Rondinelli, C.J. Fennie, Adv. Funct. Mater. 10 (2013) 4810.
[43] B. Meyer, D. Vanderbilt, Phys. Rev. B 65 (2002) 104111.
[44] J.B. Goodenough, Magnetism and the Chemical Bond, John Wiley and Sons, New York-London, 1993.